

Edit 12 May 2009

Evolution of Magnetic Fields in High Mass Star Formation: Linking field geometry and collapse for the W51 e2/e8 cores

Ya-Wen Tang

*Department of Physics, National Taiwan University, No. 1, Sec. 4, Roosevelt Road, Taipei
10617, Taiwan &*

*Academia Sinica Institute of Astronomy and Astrophysics, P. B. Box 23-141, Taipei
10617, Taiwan*

Paul T. P. Ho

*Academia Sinica Institute of Astronomy and Astrophysics, P. B. Box 23-141, Taipei
10617, Taiwan &*

*Harvard-Smithsonian Center for Astrophysics, 60 Garden Street Cambridge, MA 02138,
U.S.A.*

Patrick M. Koch

*Academia Sinica Institute of Astronomy and Astrophysics, P. B. Box 23-141, Taipei
10617, Taiwan*

Josep M. Girart

*Institut de Ciències de l'Espai (CSIC-IEEC), Campus UAB, Facultat de Ciències, Torre
C5 - parell 2, 08193 Bellaterra, Catalunya, Spain*

Shih-Ping Lai

*Academia Sinica Institute of Astronomy and Astrophysics, P. B. Box 23-141, Taipei
10617, Taiwan &*

*Institute of Astronomy and Department of Physics, National Tsing Hua University, 101,
Section 2, Kuang Fu Road, Hsinchu, Taiwan 300, R. O. C.*

Ramprasad Rao

*Submillimeter Array, Academia Sinica Institute of Astronomy and Astrophysics, 645 N.
Aohoku P1, HI 9672, USA*

ABSTRACT

We report our observational results of 870 μm continuum emission and its linear polarization in the massive star formation site W51 e2/e8. Inferred from the linear polarization maps, the magnetic field in the plane of sky (B_{\perp}) is traced with an angular resolution of $0''.7$ with the Submillimeter Array (SMA). Whereas previous BIMA observations with an angular resolution of $3''$ (0.1 pc) showed a uniform B field, our revealed B_{\perp} morphology is hourglass-like in the collapsing core near the Ultracompact H II region e2 and also possibly in e8. The decrease in polarization near the continuum peak seen at lower angular resolution is apparently due to the more complex structures at smaller scales. In e2, the pinched direction of the hourglass-like B field morphology is parallel to the plane of the ionized accretion flow traced by H53 α , suggesting that the massive stars are formed via processes similar to the low mass stars, i.e. accretion through a disk, except that the mass involved is much larger. Furthermore, our finding that the resolved collapsing cores in e2 and e8 lie within one subcritical 0.5 pc envelope supports the scenario of *magnetic fragmentation* via ambipolar diffusion. We therefore suggest that magnetic fields control the dynamical evolution of the envelope and cores in W51 e2 and e8.

Subject headings: ISM: individual (W51 e2/e8) — ISM: magnetic fields — polarization — stars: formation

1. Introduction

The magnetic (B) field has been suggested to play an important role in the star formation process. While the B field flux density is eventually redistributed via ambipolar diffusion (Mestel & Spitzer 1956; Mouschovias 1978), the collapse itself is slowed sufficiently to explain the low star formation rate observed in molecular clouds. Alternative support via turbulence (cf. Mac Low & Klessen 2004) seems less important on parsec (pc) scales since the B fields in the plane of sky (B_{\perp}) are often observed to be organized and uniform across the cloud, such as in M17 (Dotson 1996), OMC-1 (Schleuning 1998) and DR21 MAIN (Kirby 2009). One key question is at which sizescale will the magnetic support be overcome by gravity. The morphology of the B field at that point may reveal the details of the contraction process such as geometry and timescale. The Submillimeter Array (SMA) can be used to address this question by resolving the B_{\perp} structures via dust polarization studies with high angular resolutions at typically a few arcseconds.

The B field is traced by the dust continuum emission. The dust grains are most likely not spherical in shape, but somewhat elongated. They are thought to be aligned with their

minor axes parallel to the B field in most of the cases (Lazarian 2007). Among different alignment mechanisms, radiation torques seem to be a promising mechanism to align the dust grains with the B field (Draine & Weingartner 1996; Lazarian & Hoang 2007). Due to the differences in emissivity perpendicular and parallel to the direction of alignment, the observed thermal dust emission will be linearly polarized. The direction of the linear polarization is therefore perpendicular to the B field. With the SMA, we are able to detect the polarized component of the thermal dust emission at sub-millimeter (sub-mm) wavelengths in order to trace the B field within the dense cores, where stars are formed. Compared to the polarization studies via absorption and scattering of stellar light in the optical or near infrared (Goodman et al. 1995), sub-mm polarization, being derived directly from dust emission, does not suffer from a limited range in grain size and the possible contamination from the more diffuse emission and absorption along the line of sight.

In this paper, we present SMA observational results with an angular resolution of $0''.7$ (0.02 pc) of the massive star forming site W51 e2 and e8 in W51 MAIN. The dust continuum at a wavelength of $870\ \mu\text{m}$, and the B_{\perp} field inferred from its linearly polarized component are presented. The W51 MAIN is on the eastern edge of W51. It is at a distance of 7.0 ± 1.5 kpc (Genzel et al. 1981) or 6.1 ± 1.3 kpc (Imai et al. 2002). Here, we adopt a distance of 7 kpc. There is a group of Ultracompact H II (UCHII) regions in W51 MAIN, and many H_2O , OH and NH_3 maser spots have been identified (Genzel et al. 1981; Gaume & Mutel 1987; Pratap et al. 1991) to be associated with the e2 and e8 regions. The terminology of the structures discussed in this paper is shown in the schematics in Figure 1. The radio continuum sources e2, e4, e8, e1 and e3 are UCHII regions (Gaume & Johnston 1993; Zhang & Ho 1997), and their locations are labelled in Figure 2. Hereafter, *e2*, *e4*, *e8*, *e1* and *e3* (when in *italic*) refer to their corresponding UCHII regions. The infall signatures toward the e2 and e8 regions (i.e., e2 and e8 collapsing cores) have been detected clearly in NH_3 (Ho & Young 1996; Zhang & Ho 1997) and in CS (Zhang et al. 1998), indicating that they are in an early evolutionary stage. Furthermore, the total luminosity of the W51 MAIN is $2\times 10^6 L_{\odot}$ (Jaffe et al. 1987), indicating that it is a massive star forming site.

The polarized dust emissions associated with the envelope of the W51 e2 and e8 regions have been previously observed at 1.3 mm and $850\ \mu\text{m}$. The B_{\perp} field structure varies with different size scales. Chrysostomou et al. (2002) has shown that the morphology of the field on the very large scale observed with SCUBA with an angular resolution of $\sim 10''$ (0.5 pc) appears more complex, possibly because of projection effects from several clouds along the line of sight. With an angular resolution of $\sim 3''$ (0.1 pc) with the BIMA, Lai et al. (2001) found that the position angles (P.A.s) of the polarization vectors vary smoothly across the e2 and e8 cores (Figure 2(a)), suggesting that the B field dominates over the turbulent motions in the envelope. At which scales will the B field lose its dominance over turbulence and

gravity?

2. Observation

The observations were carried out on 2008 July 13 using the SMA (Ho et al. 2004)¹ in the extended configuration, with seven of the eight antennas available. The projected lengths of baselines ranged from 30 to 262 k λ . The largest size scale which could be sampled in this observation was $\sim 8''$ (0.3 pc). The local oscillator frequency was tuned to 341.482 GHz. With the 2 GHz bandwidth in each sideband, we were able to cover the frequency ranging from 345.5 to 347.5 GHz and from 335.5 to 337.5 GHz in the upper and lower sidebands, respectively. The phase center is near $e2$ at Right Ascension (J2000) = $19^h 23^m 43^s.95$, Declination (J2000) = $14^\circ 30' 34''.00$. $e8$ is $\sim 7''$ south of the phase center. The primary beam (field of view) of the SMA at 345 GHz is $\sim 30''$.

Linear polarization (LP) observations using interferometer arrays are best obtained using receivers which detect both orthogonal circular polarizations (CP) simultaneously. However, the SMA receivers are intrinsically linearly polarized and only one polarization is available currently. Thus, quarter-wave plates were installed in order to convert the LP to CP. Detailed information of the design of the quarter-wave plates and how the quarter-wave plates were controlled is described in Marrone et al. (2006) and Marrone & Rao (2008). We assume that the smearing due to the change of the P.A.s on the time scale of 5 minutes in one cycle of polarization measurement is negligible.

The conversion of the LP to CP is not perfect. This instrumental polarization (also called the leakage terms) (see Sault et al. 1996) and the bandpass were calibrated by observing 3c454.3 for 2 hours while it was transiting in order to get the best coverage of parallactic angles. The instrumental polarization is $\sim 1\%$ for the upper sideband and $\sim 3\%$ for the lower sideband before calibration, and $\sim 0.6\%$ after calibration in both sidebands. The complex gains were calibrated every 12 minutes by observing 1751+096 until it set, followed by 1925+211 for the last 3.5 hours. The absolute flux scale was calibrated using Titan.

The data were calibrated and analyzed using the MIRIAD package. After the standard gain calibration, self-calibration was also performed by selecting the visibilities with uv distances longer than 40 k λ . In order to Fourier transform the measured visibilities to the

¹The Submillimeter Array is a joint project between the Smithsonian Astrophysical Observatory and the Academia Sinica Institute of Astronomy and Astrophysics and is funded by the Smithsonian Institution and the Academia Sinica.

image, the task INVERT in MIRIAD was used with natural weighting. The Stokes Q and U maps are crucial for the derivation of the polarization. We use the dirty maps of Q and U to derive the polarization in order to avoid a possible bias introduced from the CLEAN process. We applied CLEAN to the Stokes I (total intensity) map in order to reduce the sidelobes. The presented SMA images have all been corrected for the primary beam attenuation. The synthesized beam of the presented maps is $0''.7 \times 0''.6$ with a P.A. of -58° . The presented polarization vectors are gridded to a $0''.3$ spacing - which is about half of the synthesized beam FWHM - in order to show the curvature of the B field morphology. Therefore, adjacent polarization vectors are not formally independent within one synthesized beam. However, as usual, relative information can be extracted at under the synthesized beam resolution.

The Stokes I , Q and U images of the continuum are constructed with natural weighting in order to get a better S/N ratio for the polarization. The noise levels of the I , Q and U images are ~ 60 , 4 and 4 mJy Beam $^{-1}$, respectively. The strength (I_p) and percentage ($P(\%)$) of the linearly polarized emission are calculated from: $I_p^2 = Q^2 + U^2 - \sigma_{Q,U}^2$ and $P(\%) = I_p/I$, respectively. The term $\sigma_{Q,U}$ is the noise level of the Stokes Q and U images, and it is the bias correction due to the positive measure of I_p (Leahy 1989; Wardle & Kronberg 1974). The σ_{I_p} is thus 4 mJy beam $^{-1}$. To derive the polarization, the MIRIAD task IMPOL was used. The SMA polarization vectors presented are above $3\sigma_{I_p}$ in red segments and between 2 to 3 σ_{I_p} in black segments.

3. Results

The $870 \mu\text{m}$ continuum emission and its polarized components were detected (Figure 2; Table 1 & 2). The results are presented in this section.

3.1. Continuum Emission

In $e2$, a compact $870 \mu\text{m}$ continuum emission structure with a radius of $\sim 1''$ (0.03 pc) is centered at $\sim 0''.7$ east of $e2$. Extending to the north-west of this compact emission, a fainter structure with an overall length of $\sim 2''$ (0.07 pc) is detected. The H_2O (Genzel et al. 1981) and (J,K)=(9,6) NH_3 (Pratap et al. 1991) masers are located in this north-west extension, $\sim 2''$ away from the continuum peak. Associated with the continuum peak, there are OH masers detected within $0''.5$ to the east and $\sim 1''$ to the south of $e2$ (Gaume & Mutel 1987?), suggesting that it is an active star forming site.

In $e8$, the $870 \mu\text{m}$ continuum peak is centered at $0''.3$ west of $e8$. $e4$, $e1$ and $e3$ are at the

periphery of the 870 μm continuum emission. There is an extension toward the south-west with an overall length of $\sim 3''$. Associated with *e8*, an NH_3 maser spot was detected $0''.8$ south of the 870 μm continuum peak by Pratap et al. (1991). The OH (Gaume & Mutel 1987) and H_2O (Genzel et al. 1981) masers are also associated with *e8* and the 870 μm continuum peak, suggesting again that this is an active star formation site.

When fitted with a Gaussian, the deconvolved size of the 870 μm emission in *e2* is $0''.9 \times 0''.8$, slightly larger than the synthesized beam, and therefore, the *e2* core has been resolved. For *e8*, the deconvolved size is $0''.9 \times 0''.3$ with a P.A. of 12° . Therefore, *e8* has been resolved along the major axis of the dust ridge but not along the minor axis. In both *e2* and *e8*, the 870 μm continuum emissions are associated with the NH_3 cores (Ho et al. 1983; Zhang & Ho 1997), suggesting that they are also tracing the dense regions.

The measured 870 μm flux densities within the upper and lower boxes in Figure 2(b), associated with *e2* and *e8*, are 9.3 and 4.0 Jy, respectively. The flux densities of the free-free continuum F_{ff} at 1.3 cm in *e2* and *e8* are 300 mJy (Gaume & Johnston 1993) and 17 mJy (Zhang & Ho 1997), respectively. In order to estimate the F_{ff} contribution at 870 μm , we extrapolate from 1.3 cm, assuming $F_{ff} \propto \nu^{-0.1}$. Although this assumption of optically thin emission is crude, it has been shown that the resultant F_{ff} roughly agrees (within a factor of 3) with the estimate from the radio recombination line at 2 mm (Zhang et al. 1998), suggesting that the assumed $F_{ff} \propto \nu^{-0.1}$ is reasonable. The extrapolated F_{ff} at 870 μm is ~ 230 and 13 mJy for *e2* and *e8*, respectively. As compared to the 870 μm flux densities, F_{ff} contributes $\sim 2\%$ for the *e2* region and 0.3% for the *e8* region. Therefore, the 870 μm continuum is dominated by dust emission. Hereafter, the structures traced by the 870 μm emission in the *e2* and *e8* regions are named as *e2* dust ridge and *e8* dust ridge, respectively.

Assuming a dust temperature of 100 K (Zhang et al. 1998), a dust grain emissivity $Q(\lambda) \propto \lambda^{-\beta}$ with $\beta = 1$, and the normal gas to dust ratio of 100, we estimate gas masses M_{gas} of 245 and 106 M_\odot for the *e2* and *e8* dust ridges, respectively (cf. Tang et al. 2009). Note that the M_{gas} given here is highly affected by the assumed β . If the assumed β is 2, the estimated M_{gas} will be 14 times larger. Assuming the extents along the line of sight are equal to the diameters of the emission area in the *e2* and *e8* dust ridges, the average gas number densities n_{H_2} are 3.4×10^6 and $2.2 \times 10^6 \text{ cm}^{-3}$, respectively. By using the same equation and the same assumed values of β and dust temperature, the M_{gas} estimated from the 2 mm dust continuum (Zhang et al. 1998) for the *e2* and *e8* dust ridges are 1100 and 590 M_\odot , respectively. The difference in the estimated M_{gas} at 2 mm and 870 μm is most likely due to the missing flux from the extended component, which is not recovered with our SMA observations. In comparison, with the same assumptions, the M_{gas} of the envelope is 1834 M_\odot as traced at 1.3 mm by BIMA (Lai et al. 2001). The M_{gas} associated with the *e2* and

e8 dust ridges recovered with our SMA observations is $\sim 19\%$ of the M_{gas} in the envelope.

The main conclusion from the dust continuum data is that the associated mass is large. The morphology of the dust continuum is elongated. The positional offsets between the various embedded sources are significant, such as between the positions of the $870 \mu\text{m}$ peaks and the UCHII regions. These results are consistent with the formation of a cluster of stars.

3.2. Dust Polarization

The polarization in the e2 and e8 dust ridges is detected and resolved (Figure 2 (c) and (d)). Throughout the paper, P.A. is defined from the north to the east. In the e2 dust ridge, the bulk of the polarization vectors form a ring around the $870 \mu\text{m}$ peak with a radius of $\sim 1''$ and with the geometric center near the continuum peak instead of *e2*. In the north-west extension of the dust ridge, the polarization appears to be perpendicular to the major axis of the extension.

The e8 dust ridge is $\sim 7''$ away from the phase center. Even though the antenna response is 15% less efficient than at the phase center, the polarization revealed is clearly also not as uniform as previously seen with BIMA. The polarization vectors again form a ring like structure around the continuum peak. The polarization is weaker in e8 with more vectors between 2 to $3 \sigma_{I_p}$.

In comparison, the polarization in the envelope of the e2 and e8 regions, as revealed with an angular resolution of $3''$ (0.1 pc) with BIMA, shows a relatively uniform distribution in P.A. and therefore, a fairly uniform B_{\perp} field at 1.3 mm (Figure 2(a); Lai et al. 2001). In their results, the polarization in the e2 region is weak and resolved into e2 main and e2 pol NW, named in the same paper, according to the P.A. of the polarization vectors. The component e2 pol NW is at $3''$ to the north-west of *e2*. There is a gap where no polarized emission is detected between *e2* and e2 pol NW. In the e8 region, the polarization in the BIMA results is nearly uniform with a decrease in polarization percentage near the peak position.

In order to test if the differences in polarization properties from SMA and BIMA are due to their different angular resolutions, we smoothed our SMA results to the BIMA resolution, as shown in Figure 3. Wherever the polarized emission was both detected at 1.3 mm and $870 \mu\text{m}$, the resultant P.A.s of the polarization differed by $\sim 30^\circ$ on average. This significant difference can be due to the different sampling of the visibilities, which are in the range of 6 to 170 $\text{k}\lambda$ ($\lambda=1.3 \text{ mm}$) for the BIMA and in the range of 30 to 262 $\text{k}\lambda$ ($\lambda=870 \mu\text{m}$) for the SMA. Specifically, the SMA filtered out the more extended and uniform component which is

larger than $8''$. At the same angular resolution, the derived global B_{\perp} field directions in e2 and in e8 are therefore consistent in the regions where both the SMA and BIMA have polarization detections. Most importantly, the smoothed SMA polarization map shows that the polarization percentage has decreased significantly, especially near the continuum peak positions, where the field geometry is more complex at the resolution of $0''.7$. This demonstrates that the low polarization percentage at the emission peaks is due to the limited angular resolution when a more complex underlying B field morphology has not been resolved. This effect can also be due to the decrease of the alignment efficiency of the dust grains in denser regions (Lazarian & Hoang 2007) or due to geometrical effects, such as the differences in the viewing angles (Gonçalves et al. 2005). However, in this case, the complex B field structure is the dominant effect.

The polarization percentage $P(\%)$ decreases with increasing continuum intensity I in both e2 and e8 even for the higher resolution SMA results (Figure 4). Since the BIMA results come from a resolution effect, the same might be true for the SMA results at the emission peaks. Away from the emission peaks, the general increase in $P(\%)$ is somewhat misleading. Figure 2(a) shows that this effect is not symmetrical on either side of the elongated envelope, i.e. the $P(\%)$ differs with positions on the same contour level of I . This is reflected by the large dispersion in $P(\%)$ at any value of I/I_{max} . Several effects, including B field geometry related to the line of sight, need to be disentangled. That the $P(\%)$ ranges mainly between 1% to 10% (Figure 4), seems to agree with the model of grain growth in the dense regions where grain alignments are via radiative torques (see Figure 11 in Pelkonen et al. 2009). However, based on our results, the effects of angular resolution and geometry must first be taken into account.

4. Discussion

4.1. Hourglass B field Morphology inside the e2 dust ridge?

The inferred B field in the e2 dust ridge exhibits a complex but organized morphology (Figure 5). We have tested the hypothesis of the measured B field being radial, and have shown quantitatively the preference of a non-radial field at a high significance level (see Appendix). There are positions where no polarized emission (depolarization) is detected, extending along a P.A. $\sim 60^{\circ}$ across the $870 \mu\text{m}$ peak (color scale in Figure 2(c)). The existence of non-radial field lines together with the depolarized zones are in favor of an hourglass field morphology. Along the extension of the dust ridge toward the north-west, the B field lines are approximately parallel to the major axis, which is consistent with the BIMA measurement at 1.3 mm. These lines are radial-like, but the complex structure in the

north-west could belong to another embedded source as possibly indicated by the masers.

Associated with $e2$, organized motions in the ionized gas have been revealed with the H53 α radio recombination line (Keto & Klaassen 2008), with the maximum velocity gradient along P.A. $\sim 60^\circ$. These authors interpret this gradient as a supporting evidence for an accretion flow along a dense flattened structure, where the detected motion tracks the ionized particles on the surface of the dense midplane. Both the infall and rotation near $e2$ have also been detected in several molecular lines (Ho & Young 1996; Zhang & Ho 1997; Zhang et al. 1998). As discussed in Keto & Klaassen (2008), this H53 α accretion flow in the direction of P.A. $\sim 60^\circ$ might drive the molecular outflow at P.A. $\sim -20^\circ$ as traced by the CO 2-1 line. The argument is based on the hypothesis that if the massive star formation process is similar to the low mass case, the bipolar outflow should be along the rotation axis. The linearly distributed H₂O and OH masers in the W51 $e2$ region could trace an outflow (Figure 19(c), De Buizer et al. 2005), as identified with the CO 2-1 line. Although the determined direction may be highly uncertain, the rotation in NH₃ (3,3) is more clearly revealed along PA=135 $^\circ$ (Figure 7 in Zhang & Ho 1997) and in CH₃CN along PA=110 $^\circ$ (Zhang et al. 1998), which seems inconsistent with the gradient detected with the H53 α ionized flow. This might indicate that the revealed kinematics based on different lines may be from multiple embedded sources. Higher spatial resolution kinematic studies with hot core molecular lines will be helpful for deciphering the underlying structures.

The B field appears to be hourglass-like near $e2$, with the field lines pinched along the plane of the proposed H53 α accretion disk. If the B field lines are frozen into the ionized material, the field lines will be tangled along with the rotation and infall motions. The revealed depolarization might then result from the more complex underlying B field. We note that the field lines seem to go to the core with an essentially radial pattern, and therefore, leading to a sharp pinched angle in the hourglass. In contrast, the low mass case (Girart et al. 2006) shows a wider and smoother pinched angle. We speculate that a larger infall momentum and a larger differential rotation (Zhang et al. 1998) might drag the field lines along and result in a narrower pinched angle in the projected plane. Projection of a nearly pole-on hourglass-like morphology possibly also leads to similar signatures. In any case, the scenario of material accreting through a disk as proposed by Keto and Klaassen (2008) is supported by our inferred B field morphology.

4.2. Hourglass B field Morphology in the e8 dust ridge?

Along the e8 dust ridge, the B field also shows a systematic deviation from the larger scale (0.5 pc) B field revealed by BIMA. This can again be explained by the field lines being

dragged along with the accretion toward $e8$. In this case, the revealed B field appears to be part of an hourglass structure on a larger scale of $4''$ (~ 0.08 pc) (Figure 5(b)), with its pinched direction parallel to the dust ridge. Centered on the $e8$ continuum peak, a compact hourglass structure would be more convincing except for the field lines to the north. There are H_2O masers north of the $e8$ continuum peak, and another embedded source may be indicated. This could explain the incomplete hourglass structure here.

As in the case of $e2$, a zone of depolarization seems to be present at the continuum peak, along the north-south direction. This is consistent with the pinch direction of the hourglass-like morphology being along the elongated $e8$ dust ridge. Rotation associated with the $e8$ collapsing core was detected in the direction of P.A. $\sim 156^\circ$ (-24°) with CH_3CN (Zhang et al. 1998). In this scenario, the pinch direction of the hourglass-like B field is parallel to the plane of rotation. The rotation axis of the $e8$ collapsing core is then almost parallel to the B field threading the $870 \mu\text{m}$ dust ridge. Note that the rotation direction as traced in CH_3CN is still uncertain (Zhang et al. 1998). An accurate determination of the plane of rotation associated with the $e8$ collapsing core is needed to test if the larger scale B field controls the direction of accretion.

Although the plane of accretion (or the pinched angle of the hourglass) cannot be determined with certainty, the collapse signature was detected toward $e8$ (Ho & Young 1996; Zhang & Ho 1997; Zhang et al. 1998), consistent with the possible hourglass-like B field morphology. Furthermore, this collapsing core is inside the 0.08 pc scale dust ridge, as revealed with the $0''.7$ angular resolution B field morphology. Based on this morphology and the presence of $e4$, $e8$, $e1$, and $e3$, we suggest that the star formation process involves different stages of fragmentation, proceeding at different evolutionary timescales.

4.3. Estimate of the Strength of the B field

The B field strength can be estimated by comparing the gravitational force f_G with the B field tension f_B following Dotson (1996) and Schleuning (1998). The value of f_G at a distance R_G away from the center is given by

$$f_G = \frac{G M_R \rho}{R_G^2} = 5 \times 10^{-26} \frac{M_R}{100 M_\odot} \frac{n_{\text{H}_2}}{10^5 \text{ cm}^{-3}} \left(\frac{R_G}{0.1 \text{ pc}}\right)^{-2} \frac{\text{dyne}}{\text{cm}^3}, \quad (1)$$

where M_R refers to the gas mass enclosed within a radius R_G , ρ is the mass density at R_G , and n_{H_2} is the gas volume number density. The f_B can be given by

$$f_B = \frac{1}{4\pi} \vec{B} \cdot \vec{\nabla} \vec{B} \sim \frac{B^2}{4\pi R_B} = 5 \times 10^{-26} \left(\frac{B}{\text{mG}}\right)^2 \left(\frac{R_B}{0.5 \text{ pc}}\right)^{-1} \frac{\text{dyne}}{\text{cm}^3}, \quad (2)$$

where R_B is the radius of a magnetic flux tube, and B is the B field strength. Since the e2 and e8 cores are known to be in a collapse stage, we conclude that $f_G > f_B$. An upper limit of B can then be derived. For the e2 collapsing core, M_R is estimated to be $220M_\odot$ based on the $870 \mu\text{m}$ flux density within a radius of $1''$ of the continuum peak. This is consistent with the proposed self gravitating mass of $>160 M_\odot$ (Ho & Young 1996) based on the kinematics of the NH_3 lines. R_G is $1''$ (0.034 pc), and the mean n_{H_2} within R_G is $2.7 \times 10^7 \text{ cm}^{-3}$. Assuming $R_G = R_B \simeq 0.034 \text{ pc}$, the B field strength in the e2 core is therefore $< 19 \text{ mG}$. In the e8 collapsing core, M_R is $94 M_\odot$, and n_{H_2} is $1.2 \times 10^7 \text{ cm}^{-3}$ within a radius of $1''$ centered on the peak position. The B field strength in the e8 core is therefore $< 8 \text{ mG}$. Both of the upper limits of B are consistent with the lower limit of the larger scale B_\perp field strength of 1 mG (Lai et al. 2001) estimated from the method proposed by Chandrasekhar & Fermi (1953).

4.4. Characteristic Length Scales

To analyze the interactions between B field, gravitational force and thermal force in star forming sites, we further calculate the following three length scales following Mouschovias (1991): First, the interplay between ambipolar diffusion and Alfvén waves is characterized by the Alfvén length scale λ_A . Second, the interplay between gravitational and thermal pressure forces is characterized by the thermal Jeans length scale $\lambda_{\text{T,cr}}$, following Bonnor (1956) and Ebert (1955; 1957). Third, the interplay between magnetic and gravitational forces is characterized by the critical magnetic length scale $\lambda_{\text{M,cr}}$. They can be calculated using the following equations:

$$\lambda_A = 8 \frac{B}{\text{mG}} \left(\frac{n_{\text{H}_2}}{10^6 \text{ cm}^{-3}} \right)^{-1} \left(\frac{K}{3 \times 10^{-3}} \right)^{-1} \text{ mpc}, \quad (3)$$

$$\lambda_{\text{T,cr}} = 31 \sqrt{\frac{T}{100 \text{ K}} \left(\frac{n_{\text{H}_2}}{10^6 \text{ cm}^{-3}} \right)^{-1}} \text{ mpc}, \quad (4)$$

and

$$\lambda_{\text{M,cr}} = 36 \frac{B}{\text{mG}} \left(\frac{n_{\text{H}_2}}{10^6 \text{ cm}^{-3}} \right)^{-1} \text{ mpc}. \quad (5)$$

Here, the parameter k (Eq. (6f) in Mouschovias 1991), related to the mean collision time between an ionized and a neutral particle, is assumed to be 0.5 when we derive Eq. (3), which is within the most likely range given in the reference in their paper. The factor K is related to the cosmic ionization rate. We assume $K = 3 \times 10^{-3}$ (Mouschovias 1991) following the ionization rate calculated by Nakano (1979). With the assumed k and K , the estimated fractional ionization rate is 3×10^{-9} for a number density of 10^7 cm^{-3} , which seems to be reasonable. T is the gas temperature, and n_{H_2} is the gas volume number density. B is the B

field strength. Note that T is assumed to be 100 K in both the e2 and e8 dust ridges based on the analysis of the hot core lines by Zhang, Ho & Ohashi (1997). Since these natural length scales depend on n_{H_2} and B , they are calculated separately based on the detected continuum emission with the same assumption as in §3.1. In the 1.3 mm envelope, the n_{H_2} is the mean number density within a best-fit Gaussian centered on the peak, and B is the lower limit of 1 mG. In the 870 μm dust ridges, n_{H_2} is calculated within a radius of $1''$, and B is the upper limit calculated in §4.3. The calculated natural length scales in the e2 and e8 cores are listed in Table 3.

The physical meaning of these length scales are explained clearly in Mouschovias (1991) and references therein. λ_A gives the lower limit of the scale at which the B field can sustain the structure. At the scale $R < \lambda_A$, the ambipolar diffusion between neutral and ionized particles is more efficient and the Alfvénic motion is less important. $\lambda_{\text{T,cr}}$ gives the scale where the gravitational force is equal to the thermal pressure. If an object has a size scale $R > \lambda_{\text{T,cr}}$, gravity can overwhelm the thermal pressure and collapse will start. $\lambda_{\text{M,cr}}$ gives the upper limit of the scale where the cloud can be magnetically supported along the B field direction. In a region $R > \lambda_{\text{M,cr}}$, there will be enough mass and therefore the material can collapse if there are no other supporting forces.

4.4.1. Correlation with the SMA e2 dust ridge

In the e2 dust ridge, the revealed B_{\perp} morphology is clearly pinched with a radius of $\sim 0''.8$ near *e2*, comparable to the radius of the proposed rotating flattened structure of $1''$ (Zhang & Ho 1997; Zhang et al. 1998) and the proposed ionized accretion disk of $\sim 0''.5$ (Keto & Klaassen 2008). The derived $\lambda_{\text{T,cr}}$ is $\sim 0''.2$, suggesting that at $\sim 1''$, gravity will easily overcome the thermal pressure support if there are no other supporting forces. The scale where ambipolar diffusion starts to take place (λ_A) is $\sim 0''.2$ for the e2 dust ridge, consistent with the observed pinched B_{\perp} field lines. Note that the revealed width of the depolarization zone near *e2* is narrow ($< 0''.5$), which is smaller than our synthesized beam. Higher angular resolution measurements with at least $0''.3$ resolution are needed to discriminate whether the depolarization is due to ambipolar diffusion, inefficient grain alignment or other mechanisms, such as geometrical effects. The calculated scale where the B field can sustain the structure against gravitational collapsing ($\lambda_{\text{M,cr}}$) is $0''.8$ along the field line. However, it is difficult to compare $\lambda_{\text{M,cr}}$ with the scale associated with the dust ridge, because the large scale (0.5 pc) B_{\perp} field is twisted by $\sim 45^\circ$ (Figure 2(a)) at $3''$ resolution. Observations with visibilities at both shorter and longer uv ranges are needed in order to link the B_{\perp} in the core with the field in the envelope at the same wavelength. Note that the

weak constraints on λ_A and $\lambda_{M,cr}$ result from the large range of possible B field values.

4.4.2. Correlation with the SMA e8 dust ridge

The dust continuum emission appears to be ridge-like, and the minor axis of the e8 dust ridge is approximately parallel to the 0.5 pc B_\perp field direction. The deconvolved length of the e8 dust ridge along the minor axis is barely resolved, and we adopt an upper limit to the radius of $0''.3$ along the minor axis. This is consistent with the estimated $\lambda_{M,cr} < 0''.7$, and the estimated $\lambda_{T,cr}$ of $0''.3$. This suggests that thermal pressure is significant as compared to gravity and field tension at this scale. Along the major axis, the deconvolved size is $0''.9$, which is larger than $\lambda_{T,cr}$. Furthermore, ambipolar diffusion is expected to dominate at the scale $\lambda_A < 0''.2$ in e8. Hence we expect collapse and fragmentation to occur along the ridge. This is consistent with the revealed hourglass-like B field morphology associated with the e8 collapsing core at $0''.7$ resolution and the smooth B field morphology in the envelope at $3''$ resolution. These results in the e8 core seem to be consistent with the ambipolar diffusion model (Mouschovias & Morton 1991) and suggest that the formation of the dust ridge is influenced by the B field in the envelope.

4.4.3. Connection between the BIMA 0.5 pc scale envelope and the SMA dust ridges

The main difference between the 0.5 pc envelope and the dust ridges is in the large contrast in the derived value for n_{H_2} . Nevertheless, the agreement in the estimates of λ_A and $\lambda_{M,cr}$ for the envelope and the ridge is very good, because of the lower estimates of B in the envelope. This implies that the B field support is adequate till the scale of $0''.2-1''$. The derived value of $\lambda_{T,cr}$ is larger for the envelope than for the ridge, but still smaller than the measured size of the envelope. This is also consistent with the proposed scenario that the B field provides the support against gravity at the 0.5 pc scale.

4.5. Role of B_\perp from Envelope (0.5 pc) to Collapsing Cores (0.02 pc)

The structure of the B field varies with different size scales (Figure 6).

At the $0''.7$ (0.02 pc) scale, the B field in the W51 e2 and e8 cores is not uniform. In both the e2 and e8 cores, the hourglass-like morphology suggests that at the 0.02 pc scale, gravity dominates over the B field. Our estimated collapsing M_{gas} is on the order of $100 M_\odot$ (see §4.3) in both the e2 and e8 cores, which is roughly consistent with M_{gas} estimated in

the local collapsing scenario (Ho & Young 1996; Sollins et al. 2004). The cores are therefore in the supercritical phase.

At the 0.5 pc scale, the B field in the envelope is uniform throughout the e2 and e8 dust ridges, except to the north-west of e2. Due to the small dispersion of the measured P.A.s of the polarization in the envelope, the B field is suggested to dominate over the turbulence with a strength of $\gtrsim 1$ mG by Lai et al. (2001). We further suggest that the envelope is subcritical. The reasons are: 1. B field dominates over turbulence in the envelope. 2. B field is apparently sufficient to support the envelope against gravity (§4.4.3). 3. The collapse is apparent only locally in e2 and e8 with M_{gas} in the order of $100 M_{\odot}$, so that the envelope is stable.

Based on the MHD simulations (Klessen et al. 2000), turbulent motions (cf. Mac Low & Klessen 2004) can produce an elongated envelope and can sustain the envelope from collapse. However, such elongated structures would not exhibit a preferred alignment with the B field (Heitsch et al. 2001), as it is seen here. The measured B field structures from 0.02 pc to 0.5 pc do not show an obvious necessity for turbulent support. Instead, the cloud morphology, sizescale, and B field geometry are consistent with *magnetic fragmentation* via ambipolar diffusion (Mouschovias & Morton 1991; Lizano & Shu 1989; Shu et al. 2004).

4.6. Comparison with other star formation sites

Because the collapse signatures in the W51 e2 and e8 regions are clearly detected, and the UCHII regions are still relatively compact and weak, they are in an earlier evolutionary stage as compared with the other massive star formation sites, such as G5.89–0.39 (Tang et al. 2009). In G5.89-0.39, the B field is suggested to be overwhelmed by the turbulent motions from the UCHII expansion and the molecular outflows. A more complex B_{\perp} morphology is detected (Tang et al. 2009) with a spatial resolution of 0.02 pc. In contrast to G5.89–0.39, the B_{\perp} morphologies are hourglass-like in both of the W51 e2 and e8 regions at the 0.02 pc spatial resolution, but much smoother at the 0.5 pc scale. This comparison of G5.89-0.39 and W51 e2/e8 with the same spatial resolution indicates that the role of the B field varies with the evolutionary stages of the central sources.

In the low mass star formation region NGC 1333 IRAS 4A, the hourglass shape is observed on a scale of 2400 AU (0.01 pc) and M_{gas} is $\sim 1.2 M_{\odot}$ (Girart, Rao, & Marrone 2006). In comparison, the hourglass B_{\perp} structure detected in W51 e2 is on the scale of ~ 0.03 pc ($1''$), and the mass involved is $\sim 200 M_{\odot}$. The consistency of the directions of the ionized flow and the pinched field further suggests that the stars are formed with similar

mechanisms, i.e. material is accreted through a flattened structure. The difference is that the scale and the mass involved are much larger in the massive star forming regions. At the time of publication of this paper, additional observational evidence of an hourglass B field morphology in the massive star forming core G31.41+0.31 is presented in Girart et al. (2009). This further supports the proposed similar formation mechanism as in the low mass case.

However, the massive star forming sites are much further away than the low mass regions in general. For example, W51 e2 is at 7 kpc, ~ 23 times further away than NGC 1333 IRAS 4A. Observations with higher spatial resolution are thus needed for the massive star forming regions. The closest massive star forming site is Orion BN/KL. Source I in Orion BN/KL is suggested to be in an early stage of massive star formation due to the weak and compact free-free emission (Plambeck et al. 1995). Source I is also suggested to harbor an ionized accretion disk (Reid et al. 2007). The B_{\perp} at 0.5 pc starts to exhibit a larger scale hourglass-like morphology (Schleuning 1998). The existence of the ionized disk, the uniform large scale B_{\perp} geometry and the compact free-free source all suggest that it is an analog of W51 e2/e8, but at a much closer distance. The comparison between w51 e2/e8 and Source I in Orion BN/KL may provide a clue of the B_{\perp} morphology at even higher physical resolutions.

In W51 e2/e8, we found two supercritical cores at 0.03 pc within a subcritical envelope at 0.5 pc (§4.5). At a larger scale, DR21 MAIN is suggested to have started undergoing a gravitational collapse in the central part of the cloud (Kirby 2009). Suggested by the same author, in the outer part (~ 1 pc away from the center), the cloud is still magnetically supported. That the collapsing cores formed inside a magnetically supported cloud as in W51 e2/e8, is therefore not a special case. As indicated by Vaillancourt (2009), observations of B field at the larger scales are needed to test the magnetically controlled star formation process. Shorter spacing visibilities of the SMA are needed to directly compare the field morphology of the cores with the envelope at the same wavelength of $870 \mu\text{m}$. In this paper, we have demonstrated that smaller scale B_{\perp} maps provide crucial information about the B_{\perp} field by resolving the star forming cores and by linking the field morphology with the kinematics of the molecular cloud.

5. Conclusion and Summary

To study the role of the B field in the star forming cores, we have observed and analyzed the B_{\perp} morphologies, inferred from the linearly polarized dust continuum emission, in the massive star forming site W51 e2/e8 by using the Submillimeter Array (SMA). We further compare the B_{\perp} morphologies in the dust ridges with the one in the envelope. Three different

natural length scales, namely the Alfvén length scale λ_A , thermal Jeans lengths scale $\lambda_{T,cr}$, and the magnetic length scale $\lambda_{M,cr}$, are calculated and compared to the dust ridges and envelope. Here are the summary and conclusion.

1. The 870 μm continuum and its polarization in W51 e2 and e8 are resolved with an angular resolution of $0''.7$ as observed with the SMA. The polarization in both e2 and e8 exhibit complex structures. In comparison, the polarization at 1.3 mm observed at $3''$ resolution with the BIMA revealed a uniform morphology across e2 and e8, with almost no polarization detected near the peak position in e2 (Lai et al. 2001). We conclude that low or no polarization near the emission peaks heretofore seen in the star formation regions is likely due to a more complex underlying B_{\perp} morphology (§3.2).
2. In the e2 dust ridge, the inferred B_{\perp} morphology is hourglass-like near the collapsing core, with its pinched direction parallel to the direction of the ionized accretion flow as traced by $H53\alpha$ (Keto & Klaassen 2008). The B_{\perp} here shows a similar morphology as in the low mass star formation case NGC 1333 IRAS 4A. However, the mass included in this core is ~ 200 times larger. This result shows that the B field in the e2 collapsing core plays a similar role as in the low mass star formation regions (§4.1). Higher angular resolution observations are required to test if the hourglass-like B_{\perp} morphology is preserved at smaller scale.
3. The e8 dust ridge is perpendicular to the 0.5 pc scale B_{\perp} direction as revealed with the BIMA, which suggests that the B field at 0.5 pc controls the forming process of the dust ridge. The B_{\perp} along the dust ridge exhibits a systematic deviation from the B_{\perp} at 0.5 pc scale. Associated with the e8 collapsing core, the hourglass B_{\perp} morphology is more clearly detected, suggesting that the collapsing core is formed locally inside a flattened structure (§4.2).
4. The exhibited hourglass-like B_{\perp} morphologies in the e2 and possibly the e8 dust ridges are consistent with the proposed local collapse (Ho & Young 1996; Sollins et al. 2004) instead of the global collapse (Rudolph et al. 1990). This indicates that both the e2 and e8 cores are in a supercritical stage (gravity dominating over the B field) at the 0.02 pc scale. In contrast, the B field morphology of the 0.5 pc envelope is uniform across the e2 and e8 dust ridges and strong (≥ 1 mG). We further propose that the B field in the 0.5 pc scale envelope is subcritical (B field dominating the gravity). That the supercritical cores formed inside a subcritical envelope seems to support a *magnetic fragmentation* scenario (Mouschovias & Morton 1991; Lizano & Shu 1989; Shu et al. 2004), suggesting that ambipolar diffusion plays a key role in the evolution of the envelope at this stage (§4.5).

Acknowledgement The authors are grateful for the anonymous referee’s comments, which helped to improve the manuscript.

Appendix

In order to test how significantly the measured B field deviates from a purely radial field, we have analyzed the differences, δ , between position angles (P.A.s) of the measured B field lines and the corresponding hypothetical radial field lines. The radial field lines are derived from their relative positions (center of each P.A.) with respect to the origin, which is defined as the 870 μm peak in e2. Due to the limited detected data points, we do not apply this statistical analysis to e8. All the data considered are above $3 \sigma_{I_p}$. We have excluded the 6 data points in the north-west extension, which correspond to e2 pol NW. The distribution of δ apparently deviates from a Gaussian (Figure A1(Left-panel)). When, nevertheless enforcing a Gaussian fitting, the derived mean μ is 1.6° and the standard deviation σ is 14° , which is larger than the mean measurement uncertainty $\sigma_{\text{mean,PA}}$ of 6.9° .

To quantify the deviation from a Gaussian, we further apply a Kolmogorov-Smirnov (KS) test to δ . As null hypothesis we assume that the distribution of δ is normal with $\sigma_{\text{mean,PA}}$ and $\mu = 0^\circ$. This mimics an observation of a radial field with our observed measurement uncertainty $\sigma_{\text{mean,PA}}$. The measurement uncertainties in each P.A. are propagated with a Monte-Carlo (MC) simulation when deriving δ and applying the KS test. In the MC simulation we also allow for a shift of $\pm 0''.1$ of the origin of the radial field. Figure A1 (Right-panel) shows the cumulative distributions which are used for the statistic measure in the KS test. As a result, the probability of the measured field being radial is 20%. For the $\pm 1\sigma_{\text{mean,PA}}$ error bounds, the probability of being radial is less than 5%. Therefore, the null hypothesis can be rejected. Our test favors the existence of a non-radial B field.

δ as a function of P.A. is presented in Figure A2. If we separate the segments according to the depolarization zones (marked as arrows in Figure A2), there are always segments with δ larger than $3 \sigma_{\text{mean,PA}}$ in each zone. This suggests that deviations are not prevalent in certain directions, but rather grouped together and interleaved with depolarization zones, as we would expect from an hourglass field morphology.

REFERENCES

- Bonnor, W. B. 1956, MNRAS, 116, 351
 Chandrasekhar, S., & Fermi, E. 1953, ApJ, 118, 113

- Chrysostomou, A., Aitken, D. K., Jenness, T., Davis, C. J., Hough, J. H., Curran, R., & Tamura, M. 2002, *A&* 385, 1014
- De Buizer, J. M., Radomski, J. T., Telesco, C. M., & Piña, R. K. 2005, *ApJS*, 156, 179
- Dotson, J. 1996, *ApJ*, 470, 566
- Draine, B. T., & Weingartner, J. C. 1996, *ApJ*, 470, 551
- Ebert, R. 1955, *Zs. Ap.*, 37, 217
- Ebert, R. 1957, *Zs. Ap.*, 42, 263
- Gaume, R. A., & Mutel, R. L. 1987, *ApJS*, 65, 193
- Gaume, R. A., & Johnston, K. J. 1993, *ApJ*, 417, 645
- Genzel, R., Downes, D., Schneps, M. H., Reid, M. J., Moran, J. M., Kogan, L. R., Kostenko, V. I., Matveenko, L. I., Ronnang, B. 1981, *ApJ*, 247, 1039
- Girart, J. M., Rao, R., & Marrone, D. P. 2006, *Sci.*, 313, 812
- Girart, M. M., Beltran, M. T., Zhang, Q., Estalella, R., & Rao, R. 2009, in press
- Gonçalves, J., Galli, D., & Walmsley, M. 2005, *A&A*, 430, 979
- Goodman, A. A., Jones, T. J., Lada, E. A., & Myers, P. C. 1995, *ApJ*, 448, 748
- Heitsch, F., Zweibel, E. G., Mac Low, M.-M., Li, P., & Norman, M. 2001, *ApJ*, 561, 800
- Ho, P. T. P., Genzel, R. & Das, A. 1983, *ApJ*, 266, 596
- Ho, P. T. P., & Young, L. M. 1996, *ApJ*, 472, 742
- Ho, P. T. P., Moran, J. M., Lo, K. Y. 2004, *ApJ*, 616, L1
- Imai, H., Deguchi, S., Fujii, T., Glass, I. S., Ita, Y., Izumiura, H., Kameya, O., Miyazaki, A., Nakada, Y., Nakashima, J.-I. 2002, *PASJ*, 54, 741
- Jaffe, D. T., Genzel, R., Harper, D. A., Harris, A. I., & Ho, P. T. P. 1987, in *IAU Symp.* 115, *Star Forming Regions*, ed. M. Peimbert & J. Jugaku (Dordrecht: Reidel), 143
- Keto, E. & Klaassen, P. 2008, *ApJ*, 678, L109
- Kirby, L. 2009, *ApJ*, 694, 1056

- Klessen, R. S., Heitsch, F., & Mac Low, M.-M. 2000, *ApJ*, 535, 887
- Lai, S.-P., Crutcher, R. M., Girart, Josep M., & Rao, Ramprasad 2001, *ApJ*, 561, 864
- Lazarian, A. 2007, *Journal of Quantitative Spectroscopy & Radiative Transfer*, 106, 255
- Lazarian, A., & Hoang, T. 2007, *MNRAS*, 378, 910
- Leahy, P. 1989, *VLA Scientific Memoranda* 161 (Socorro: VLA)
- Lizano, S., & Shu, F. H. 1989, *ApJ*, 342, 834
- Mac Low, M.-M., & Klessen, R. S., 2004 *Rev. Mod. Phys.*, 76, 125
- Marrone, D. P., Moran, J. M., Zhao, J.-H., & Rao, R. 2006, *ApJ*, 640, 308
- Marrone, D. P., & Rao, R. 2008, in *Millimeter and Submillimeter Detectors and Instrumentation for Astronomy IV.*, ed. W. D. Duncan, W. S. Holland, S. Withington, & J. Zmuidzinas (Proceedings of the SPIE), 7020, p. 70202B-70202B-8 (arXiv:0807.2255)
- Mestel, L., & Spitzer, L. 1956, *MNRAS*, 116, 503
- Mouschovias, T. CH., & Morton, S. 1991, 371, 296
- Mouschovias, T. Ch. 1991, *ApJ*, 373, 169
- Mouschovias, T. ch. 1978, in *Protostars and Planets*, ed. T. Gehrels (Tucson: University of Arizona Press), p. 209
- Nakano T. 1979, *PASJ*, 31, 697
- Pelkonen, V.-M., Juvela, M. & Padoan, P. 2009, arXiv:0901.0831v2
- Plambeck, R. L., Wright, M. C. H., Mundy, L. G., & Looney, L. W. 1995, *ApJ*, 455, L189
- Pratap, P., Menten, K. M., Reid, M. J., Moran, J. M., & Walmsley, C. M. 1991, *ApJ*, 373, L13
- Reid, M. J., Menten, K. M., Greenhill, L. J., & Chandler, C. J. 2007, *ApJ*, 664, 950
- Rudolph, A., Welch, W. J., Palmer, P., & Dubrulle, B. 1990, *ApJ*, 363, 528
- Sault, R. J., Hamaker, J. P., & Bregman, J. D. 1996, *A&AS*, 117, 149
- Schleuning, D. A. 1998, *ApJ*, 493, 811

- Shu, F. H., Li, Z.-Y., & Allen, A. 2004, *ApJ*, 601, 930
- Sollins, P. K., Zhang, Q., & Ho, P. T. P. 2004, *ApJ*, 606, 943
- Tang, Y.-W., Ho, P. T. P., Girart, J. M., Rao, R., Koch, P., & Lai, S.-P. 2009, *ApJ*, 695, 1399
- Vaillancourt, J. E. 2009, in *Astronomical Polarimetry 2008: Science from Small to Large Telescopes*, eds. P. Bastien and N. Manset ([astro-ph://arXiv:0904.1979](https://arxiv.org/abs/0904.1979))
- Wardle, J. F. C., & Kronberg, P. P. 1974, *ApJ*, 194, 249
- Zhang, Q., & Ho, P. T. P. 1997, *ApJ*, 488, 241
- Zhang, Q., Ho, P. T. P., & Ohashi, N. 1998, *ApJ*, 494, 636

Table 1. SMA dust polarization at $870\mu\text{m}$ in e2

Δx	Δy	I	$P(\%)$	I_p	$\phi(^{\circ})$
-1.2	2.4	0.32	5.9 ± 1.1	19	66 ± 6
-1.5	2.4	0.29	6.6 ± 1.3	19	61 ± 6
-0.6	2.1	0.24	7.4 ± 1.5	18	-71 ± 6
-0.9	2.1	0.36	4.4 ± 1.0	16	-75 ± 7
0.3	1.8	0.31	4.8 ± 1.2	15	-75 ± 7
0.0	1.8	0.45	4.2 ± 0.8	19	-82 ± 6
-0.3	1.8	0.41	4.9 ± 0.9	20	-89 ± 6
-0.6	1.8	0.43	3.7 ± 0.9	16	-84 ± 7
-0.9	1.8	0.43	3.0 ± 0.9	13	-70 ± 8
0.6	1.5	0.22	5.1 ± 1.7	11	-61 ± 10
0.3	1.5	0.66	2.9 ± 0.6	19	-74 ± 6
0.0	1.5	0.96	2.3 ± 0.4	22	-87 ± 5
-0.3	1.5	0.82	2.2 ± 0.5	18	79 ± 6
0.3	1.2	1.33	0.9 ± 0.3	12	-71 ± 9
0.0	1.2	1.71	0.7 ± 0.2	12	-83 ± 9
-0.6	1.2	1.23	1.3 ± 0.3	16	19 ± 7
-0.9	1.2	0.56	3.2 ± 0.7	18	-3 ± 6
-0.3	0.9	2.67	0.6 ± 0.2	16	17 ± 7
-0.6	0.9	1.71	1.4 ± 0.2	24	9 ± 4
-0.9	0.9	0.82	2.8 ± 0.5	23	-5 ± 5
-1.2	0.9	0.21	7.5 ± 1.8	16	-18 ± 7
0.9	0.6	0.30	4.7 ± 1.3	14	18 ± 8
0.6	0.6	1.30	1.0 ± 0.3	13	37 ± 8
-0.3	0.6	2.33	0.6 ± 0.1	14	6 ± 8
-0.6	0.6	1.55	1.1 ± 0.2	17	-2 ± 6
-0.9	0.6	0.70	2.7 ± 0.6	19	-22 ± 6
0.9	0.3	0.20	7.5 ± 1.9	15	32 ± 7
0.6	0.3	0.81	2.7 ± 0.5	22	48 ± 5
0.3	0.3	1.75	0.8 ± 0.2	14	65 ± 8
-0.9	0.3	0.32	3.7 ± 1.1	12	-27 ± 9
0.6	0.0	0.22	8.1 ± 1.7	18	55 ± 6

Table 1—Continued

Δx	Δy	I	$P(\%)$	I_p	$\phi(^{\circ})$
0.3	0.0	0.60	2.5 ± 0.6	15	80 ± 7
0.0	0.0	0.95	2.1 ± 0.4	20	-79 ± 5
-0.3	0.0	0.76	1.7 ± 0.5	13	-80 ± 9
0.0	-0.3	0.23	6.0 ± 1.6	14	-81 ± 8
-3.6	-2.4	0.22	5.0 ± 1.7	11	-17 ± 10

Note. — Δx & Δy : offsets in arcsecond from Right Ascension (J2000) = $19^{\text{h}}23^{\text{m}}43^{\text{s}}.95$, Declination (J2000) = $14^{\circ}30'34''00$. I : intensity of the Stokes I component in Jy beam^{-1} . $P(\%)$: polarization percentage, derived from the ratio I_p/I . I_p : the polarized intensity in mJy beam^{-1} . ϕ : position angle from the north to the east. Listed data points are within the red box associated with $e2$ in Figure 2. All listed points are above $3 \sigma_{I_p}$.

Table 2. SMA dust polarization at $870\mu\text{m}$ in $e8$

Δx	Δy	I	$P(\%)$	I_p	$\phi(^{\circ})$
-0.6	-5.1	0.28	4.0 ± 1.3	11	76 ± 10
-1.2	-5.4	0.64	2.2 ± 0.6	14	-1 ± 8
-1.5	-5.7	0.22	5.8 ± 1.8	13	-1 ± 9
-0.9	-6.0	1.57	0.7 ± 0.2	11	-70 ± 10
-1.5	-6.6	0.27	7.5 ± 1.4	20	-21 ± 5
-1.5	-6.9	0.39	3.8 ± 1.0	15	-19 ± 7
-1.2	-7.2	0.55	2.0 ± 0.7	11	36 ± 10
-1.2	-7.5	0.42	3.3 ± 0.9	14	59 ± 8
1.5	-8.7	0.26	4.2 ± 1.4	11	6 ± 10
-1.8	-8.7	0.24	5.0 ± 1.6	12	-33 ± 9
-2.1	-8.7	0.23	8.0 ± 1.7	18	-40 ± 6
-2.1	-9.0	0.23	4.7 ± 1.5	11	-33 ± 10

Note. — Identical notation as in Table 1. Δx and Δy are with respect to the same coordinate as in Table 1. Listed data points are all within the red box associated with $e8$ in Figure 2.

Table 3. Derived parameters in e2 and e8

Parameters	units	e2		e8	
		BIMA ^a	SMA ^b	BIMA ^a	SMA ^b
$\theta_{maj} \times \theta_{min}$	"	3.6×2.6	0.9×0.8	5.0×2.2	0.9×0.3
M_R	M_\odot	-	220	-	94
n_{H_2}	cm^{-3}	1.5×10^6	2.7×10^7	7.6×10^5	1.2×10^7
B	mG	≥ 1	< 19	≥ 1	< 8
λ_A	mpc	≥ 5	< 6	≥ 11	< 5
	(")	(≥ 0.2)	(< 0.2)	(≥ 0.3)	(< 0.2)
$\lambda_{T,cr}$	mpc	25	6	36	9
	(")	(0.8)	(0.2)	(1.1)	(0.3)
$\lambda_{M,cr}$	mpc	≥ 24	< 25	≥ 47	< 24
	(")	(≥ 0.7)	(< 0.8)	(≥ 1.4)	(< 0.7)

^aThe derived mean n_{H_2} is based on a Gaussian fit of the 1.3 mm continuum emission toward the peak. All the natural length scales depend on this n_{H_2} .

^bThe derived mean n_{H_2} is within a radius of 1" centered on the 870 μm continuum peak, where the collapsing signatures were clearly revealed with the molecular lines. All the natural length scales and the upper limit of B depend on this n_{H_2} .

Note. — θ_{maj} and θ_{min} refer to the major and minor axis of the deconvolved size, respectively. They are determined by a best-fit Gaussian of the continuum emission centered on the peak. M_R refers to the estimated M_{gas} from the continuum emission within a radius of 1" centered on the peak position. The lower limit of the B field strength of 1 mG is adopted from Lai et al. (2001). Characteristic length scales λ_A , $\lambda_{T,cr}$ and $\lambda_{M,cr}$ are calculated assuming $T = 100$ K. Note that the weak constraints on λ_A and $\lambda_{M,cr}$ result from the large possible range of B field strength.

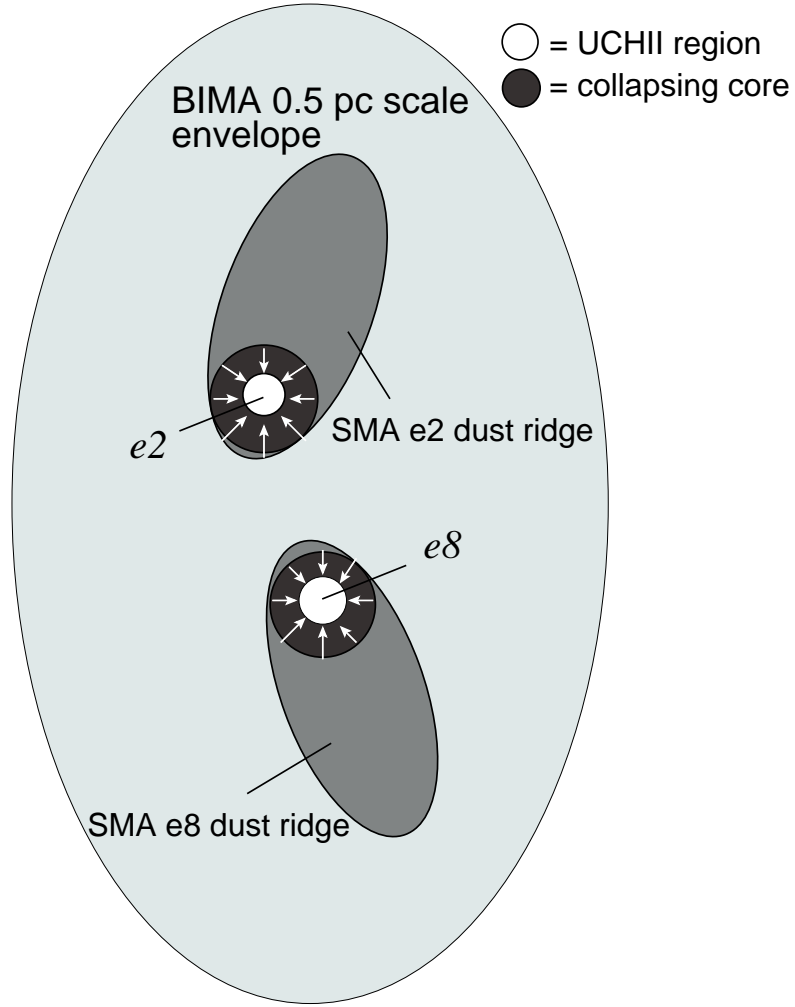


Fig. 1.— Schematic cartoon of structures in W51 $e2/e8$. $e2$ and $e8$ refer to the UCHII region $e2$ and $e8$, respectively.

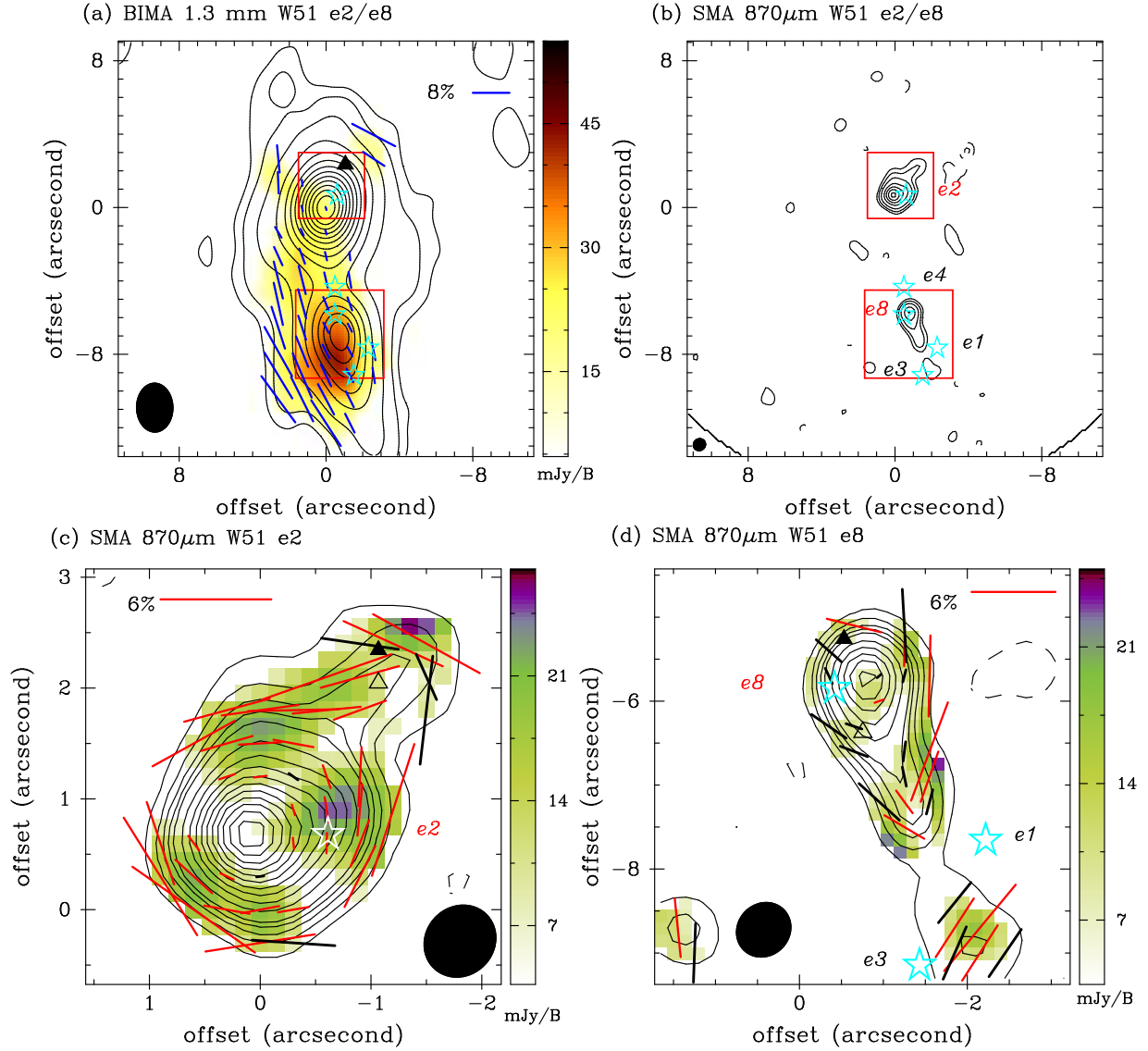


Fig. 2.— (a) Polarization map observed with BIMA adopted from Lai et al. (2001). Contours are the 1.3 mm continuum strength of $-3, 3, 5, 10, 20, 30, \dots, 90, 100, 110 \times 27 \text{ mJy beam}^{-1}$, where the size of the synthesized beam is $2''.7 \times 2''.0$. The cyan stars mark the UCHII regions. The offset is in arcsecond with respect to Right Ascension (J2000)= $19^h23^m43^s.95$, Declination (J2000)= $14^\circ30'34''.00$. Red boxes indicate the regions presented in panel (c) and (d). (b): SMA $870 \mu\text{m}$ continuum emission in W51 e2/e8. Contours are the $870 \mu\text{m}$ continuum strength at $-6, -3, 3, 6, 12, 24, 36, 48, 60 \times 60 \text{ mJy beam}^{-1}$, where the beam size is $0''.7 \times 0''.6$. All the other symbols are identical to the ones in (a). (c): SMA polarization in W51 e2. Contours are the $870 \mu\text{m}$ continuum strength at $-4, -2, 2, 4, 6, 8, 10, 15, 20, \dots, 55, 60 \times 60 \text{ mJy beam}^{-1}$. Black and red segments represent the polarization with its length proportional to the polarized percentage at 2 to $3 \sigma_{I_p}$ and above $3 \sigma_{I_p}$, respectively. Solid and unfilled triangles mark the positions of the H_2O (Genzel et al. 1981) and $(J,K) = (9,6)$ NH_3 (Pratap et al. 1991) masers, respectively. All the other symbols are identical to the ones in (a). (d) SMA polarization map in W51 e8. All the symbols and contour levels are identical to the ones in (c). All images shown have been corrected for the effect of primary beam attenuation. In each panel, the synthesized beam is plotted as a black ellipse at the lower-left corner. In panel (a), (c) and (d), the polarized intensity is shown in color scale with strength indicated by the wedge on the right in units of mJy beam^{-1} (mJy/B).

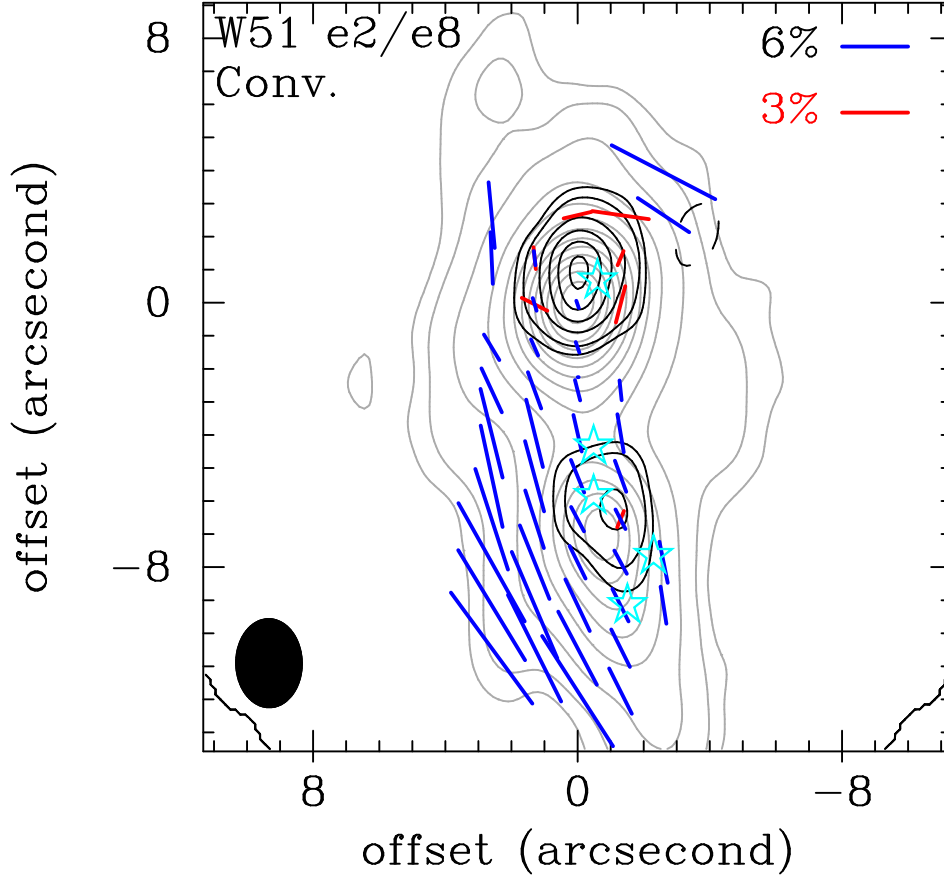


Fig. 3.— Polarization map of the SMA results (red segments) at $870\ \mu\text{m}$ restored with the BIMA synthesized beam. BIMA polarization at $1.3\ \text{mm}$ is shown in blue segments. The synthesized beam size is $2''.7 \times 2''.0$ with a P.A. of 1° . The black contours represent the SMA $870\ \mu\text{m}$ continuum emission after restoring to the BIMA resolution with contours of $-3, 3, 5, 10, 15, 20, 25 \times 0.3\ \text{Jy beam}^{-1}$. The grey contours represent the BIMA $1.3\ \text{mm}$ continuum emission with strengths as shown in Figure 2. All polarization vectors plotted are above $3\sigma_{I_p}$. All the other notations are identical to the ones in Figure 2. The slight offset between the SMA and BIMA maps is most likely due to missing short spacing information in the SMA data, being insensitive to structures larger than $8''$.

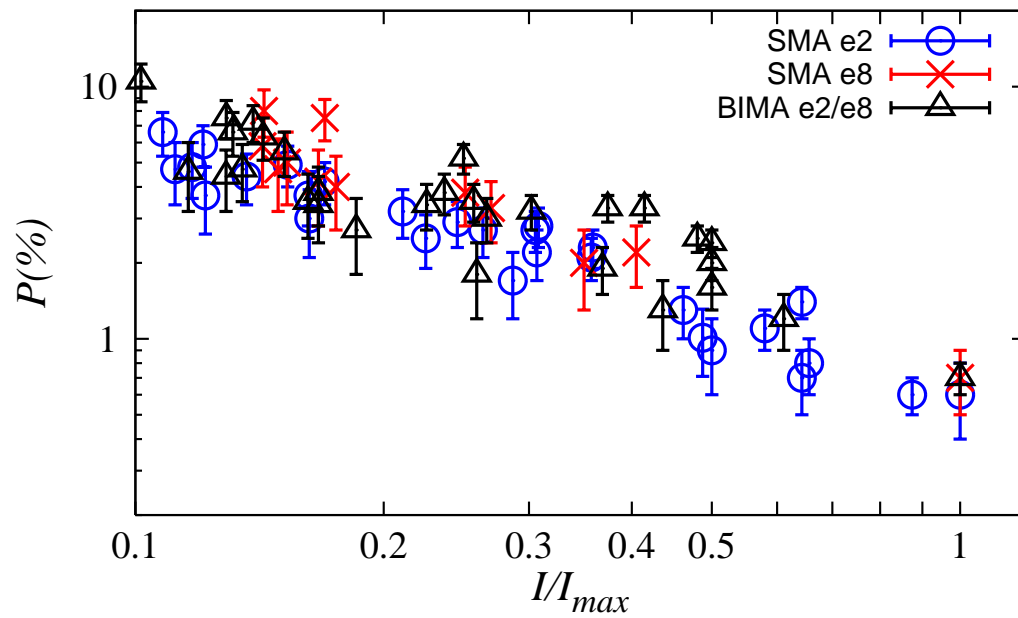


Fig. 4.— Plot of polarization percentage, $P(\%)$, versus normalized intensity (I/I_{max}). The blue circles, red crosses, and black triangles are SMA results for e2, e8 and BIMA results for both e2 and e8, respectively. All the plotted data are above $3\sigma_{I_p}$.

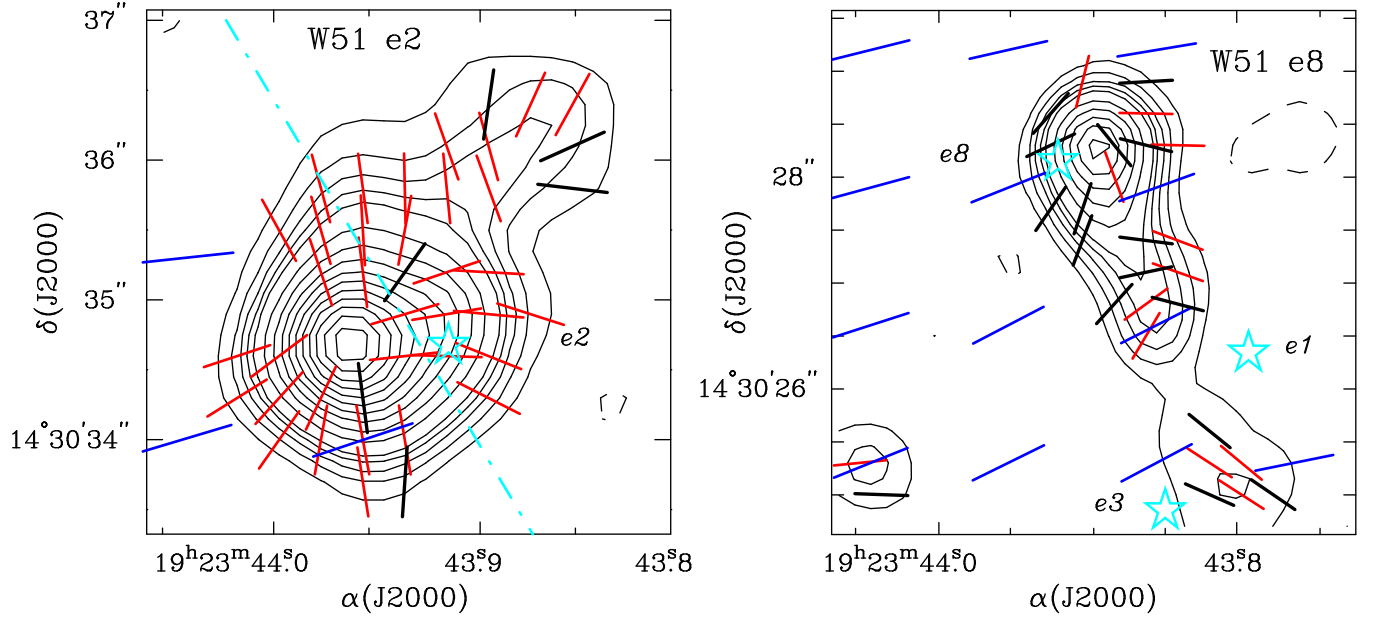


Fig. 5.— Left-panel: B field maps in W51 e2 with S/N ratio between 2 to $3 \sigma_{I_p}$ (black segments) and $>3 \sigma_{I_p}$ (red segments), and $870 \mu\text{m}$ continuum emission in black contours. The dot-dash cyan segment marks the direction of the ionized accreting flow by Keto & Klaassen (2008). Blue segments are the inferred B field direction from the BIMA. The magnetic field segments (all of equal length) are rotated by 90° with respect to the polarization segments. Right-panel: B field map in W51 e8. All the symbols are identical to the ones in the left-panel. All the contours are plotted with the same level as in Figure 2(c) and 2(d) for left-panel and right-panel, respectively. Note that even at 2 to $3 \sigma_{I_p}$, the B field directions are varying in a coherent manner. Hence the trends are significant.

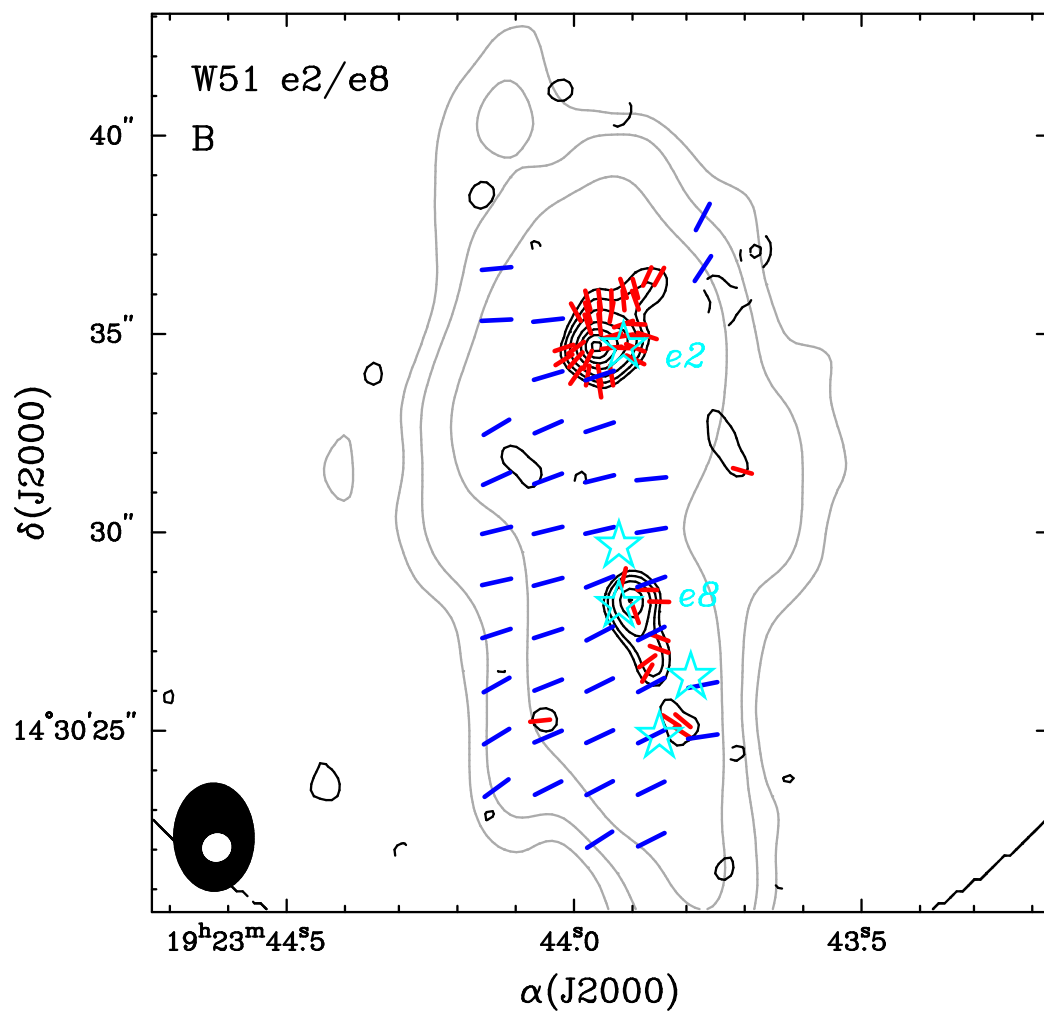


Fig. 6.— B field maps of W51 e2/e8 from the SMA (red segments) at $870\ \mu\text{m}$ and BIMA (blue segments) at $1.3\ \text{mm}$. The black and grey contours represent the strengths of the continuum emission at $870\ \mu\text{m}$ and at $1.3\ \text{mm}$, respectively. The black contours are plotted in the same levels as in Figure 2(b), and grey contours plotted are $3, 5, 10 \times 27\ \text{mJy beam}^{-1}$. The other symbols are identical to the ones in Figure 2. The synthesized beams of the SMA and BIMA are plotted in the lower-left corner as white and black ellipses, respectively.

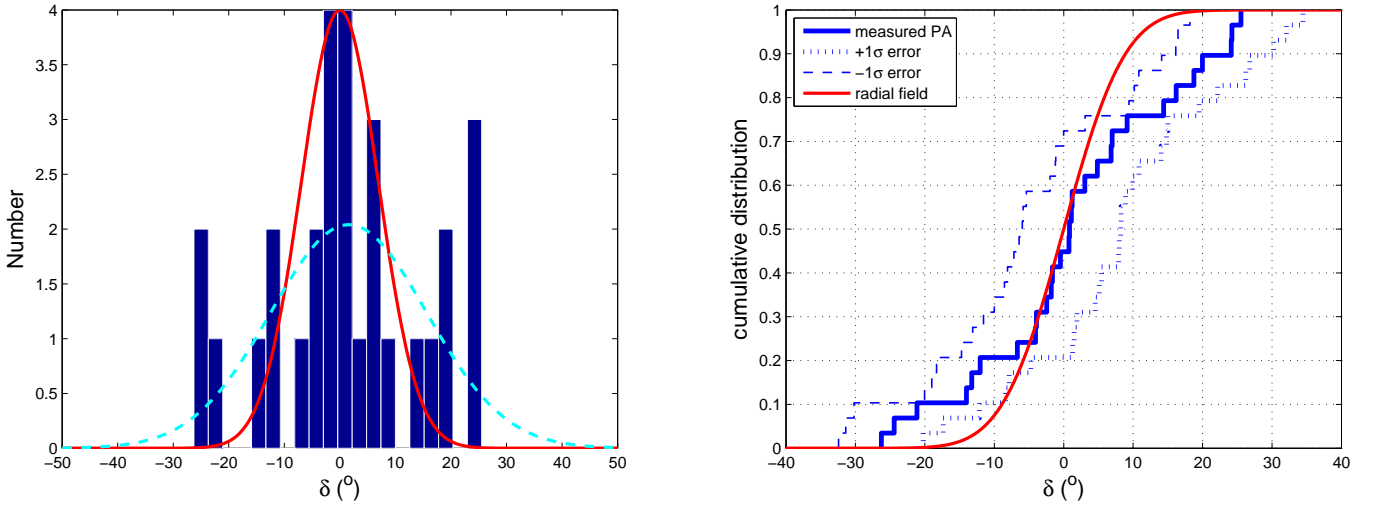


Fig. A1.— Left-panel: Histogram of the differences δ between the measured P.A. and a radial field. The cyan dashed curve is the enforced fitted Gaussian to the measurement with the resultant standard deviation $\sigma=14^\circ$ and mean $\mu=1.6^\circ$. The red solid curve is the normal distribution with $\sigma = \sigma_{\text{mean,PA}}=6.9^\circ$, which is the mean uncertainty of the measurement. Right-panel: Cumulative distribution of δ (solid blue line). The red curve marks the cumulative normal distribution with $\sigma_{\text{mean,PA}}$. The $\pm 1 \sigma_{\text{mean,PA}}$ error bounds from the MC simulation, including measurement uncertainties and the shift of the center of the radial field, are also shown.

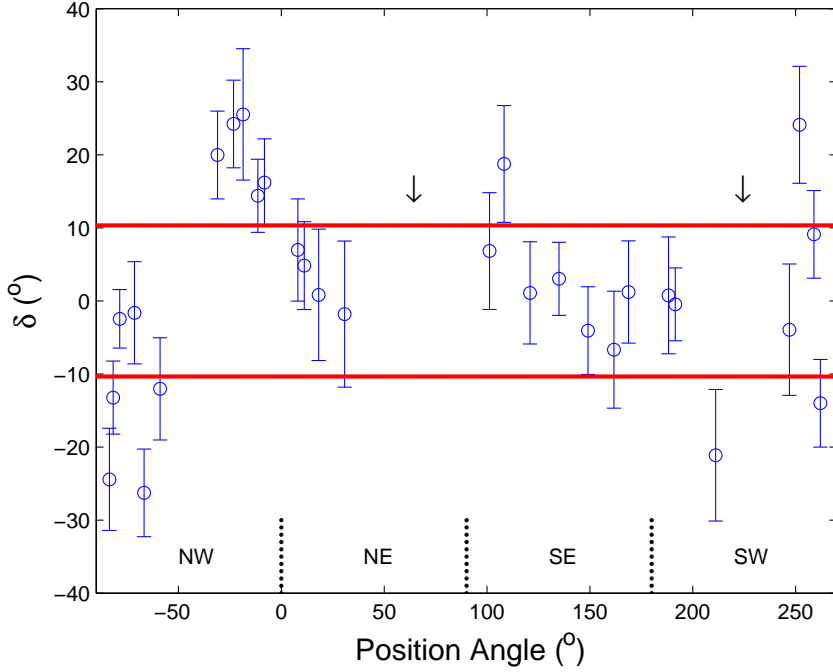


Fig. A2.— Plot of position angle versus δ . The red lines mark the $3 \sigma_{\text{mean,PA}}$ bounds. The black arrows mark the depolarization zones around P.A.s of 60° and 220° , \sim parallel to the maximum velocity gradient in the H53 α line. The areas with respect to the 870 continuum peak are marked as NW, NE, SE and SW, which correspond to the north-west, north-east, south-east and south-west, respectively. There are always $\delta > 3 \sigma_{\text{mean,PA}}$ in the areas separated by the depolarization zones.